4th Flow Control Conference
23 - 26 June 2008, Seattle, Washington

AIAA 2008-3862

Towards Feedback Control of High–Speed and High–Reynolds Number Jets

Aniruddha Sinha*, Kihwan Kim†, Jin-Hwa Kim‡, Andrea Serrani§, and Mo Samimy**
Gas Dynamics and Turbulence Laboratory, The Ohio State University, Columbus, OH, 43235

We present a first attempt and preliminary results on the development and application of feedback control to high-speed and high Reynolds number axisymmetric jets. In particular, we demonstrate control authority on the near pressure field of a Mach 0.9 jet with a Reynolds number based on jet diameter of 7.8×10^5. Open-loop forcing experiments are presented wherein our in-house developed plasma actuators are shown to have two distinct effects on the near pressure field. At low forcing Strouhal numbers (St_{DF}'s) near the jet column mode instability, a sharp peak in the pressure fluctuations is observed. At higher St_{DF}'s (close to the initial-shear-layer instability) a broad minimum is observed in the near-field pressure fluctuations, and especially in its axisymmetric mode. An online gradient-based extremum-seeking feedback control scheme is implemented; it uses the RMS of the azimuthal-mode-filtered pressure fluctuations to optimize the St_{DF}. The actual cost function for optimization can be selected as the RMS of various individual pressure azimuthal modes, or a combination thereof. The controller can be setup to either seek a maximum or a minimum with negligible reconfiguration. Preliminary experimental results are presented to demonstrate satisfactory performance in both operating regimes. Starting from either side of the minimum or maximum, the controller is shown to drive the St_{DF} to the respective optimum and maintain the value over time.

Nomenclature

a	=	perturbation amplitude in the extremum–seeking control loop
D	=	jet nozzle exit diameter
dc	=	duty-cycle
f	=	spectral frequency
f_F	=	forcing frequency
$\overline{f}$	=	nominal forcing frequency in closed-loop
$\tilde{f}$	=	error in estimation of optimum forcing frequency in closed-loop
f_F^0	=	initial value of forcing frequency in the extremum–seeking control loop
f_F*	=	optimum forcing frequency
f_n	=	most amplified initial shear layer frequency
f_p	=	jet's preferred-mode or column-mode frequency
h	=	static map from input forcing frequency to output RMS of a selected pressure azimuthal mode
k_{es}	=	gain parameter in the extremum–seeking control loop
$LAFPA$	=	localized arc filament plasma actuator
m_p	=	azimuthal mode number of pressure in the near-field (see Appendix)
m_f	=	azimuthal mode number of forcing
N_f	=	number of actuators arranged in a symmetric azimuthal array at the jet lip
N_p	=	number of pressure sensors arranged in a symmetric azimuthal array in the jet near-field

* Graduate Student, Gas Dynamics and Turbulence Laboratory, AIAA Student Member.
† Postdoctoral Researcher, Gas Dynamics and Turbulence Laboratory, AIAA Member.
‡ Research Associate, Gas Dynamics and Turbulence Laboratory, AIAA Member.
§ Assistant Professor, Dept. of Electrical and Computer Engineering, AIAA Member.
** The Howard D. Winbigler Professor of Engineering, Director of Gas Dynamics and Turbulence Laboratory, Dept. of Mechanical Engineering, AIAA Associate Fellow, Corresponding author, samimy.1@osu.edu

$OASPL$ = overall sound pressure level
p_k = pressure signal from k^{th} pressure sensor in the near-field azimuthal ring array; $k = 1, \ldots, 8$
$p^{[m_p]}$ = near–field pressure signal filtered at azimuthal mode m_p (see Appendix)
r = tip-circle radius of near-field pressure azimuthal ring array
$\mathrm{RMS}(p^{[m_p]})$ = root mean square of near–field pressure signal filtered at azimuthal mode m_p
Re_D = Reynolds number based on jet nozzle exit diameter and exit velocity
SPL = sound pressure level
St_D = Strouhal number based on spectral frequency and nozzle exit diameter = fD/U_j
St_{DF} = Strouhal number based on forcing frequency and nozzle exit diameter = $f_F D/U_j$
St_θ = Strouhal number based on the boundary layer momentum thickness at the nozzle exit = $f\theta_0/U_\infty$
U_j = jet exit velocity
U_∞ = freestream velocity for a planar free shear layer
x = streamwise distance downstream from nozzle exit
Δf_F = perturbation of forcing frequency in the extremum–seeking control loop
ΔOASPL = difference in OASPL in a forced case compared to the unforced baseline case
θ_0 = boundary layer momentum thickness at the nozzle exit or at the trailing edge of a splitter plate
θ_k = azimuthal location of k^{th} pressure sensor on the azimuthal ring array
ξ_i = internal signals in the extremum–seeking control loop shown in Figure 9, $i = 1, 2, 3, 4$
ω_a = perturbation frequency in the extremum–seeking control loop
ω_h = high-pass filter cutoff frequency in the extremum–seeking control loop
ω_l = low-pass filter cutoff frequency in the extremum–seeking control loop

I. Introduction

WE present a first attempt at feedback control of a high-speed high-Reynolds number jet. In particular, we demonstrate control over the near-field pressure with two different goals. We can either increase the pressure fluctuations for mixing enhancement, or decrease the fluctuations for potential far-field noise attenuation. In this section we will motivate the discussion and establish the background.

A. Motivation

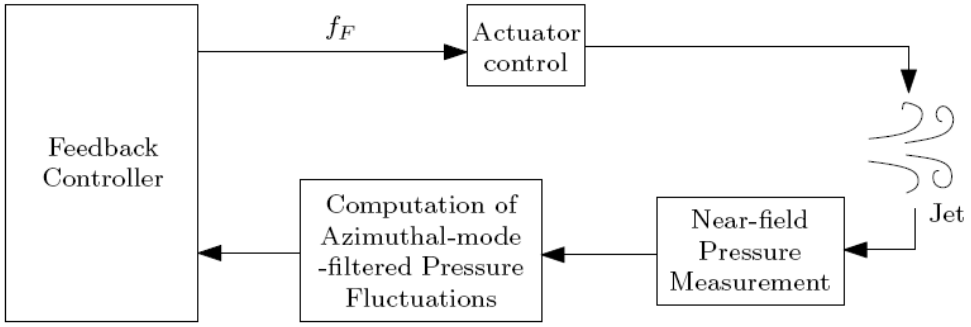

Figure 1. Feedback control system for jets using plasma actuators.

We implemented the feedback control strategy shown in Figure 1. An axisymmetric jet was operated at Mach 0.9 and the Reynolds number based on the jet nozzle exit diameter was $Re_D = 7.6 \times 10^5$. The jet was forced using an in-house developed plasma actuator system consisting of eight azimuthally placed electrode pairs at the jet nozzle exit. Each actuator generates square-pulse-like localized heating with fixed amplitude but the forcing frequency, the azimuthal mode, as well as the duty cycle can be independently controlled. Details of the actuators and their application are given in Samimy et al. (2007a & b). The forcing frequency was chosen as the control input for implementing the feedback controller. The near-field pressure was measured using an azimuthal ring array of eight transducers. The azimuthal-mode-filtered pressure fluctuation level was estimated in real-time and supplied to the feedback controller. The latter, in turn, supplied the appropriate forcing frequency to the actuators based on an online gradient-based extremum-seeking optimization algorithm. The control scheme used can be setup either to seek the maximum fluctuation level (corresponding to mixing enhancement) or the minimum level (corresponding

to potential noise attenuation). In the rest of this section, each of the choices made above will be rationalized based on previous research.

B. The Axisymmetric Jet Mixing Layer and Far-field Noise

A planar free shear layer is known to be unstable and act like an amplifier of disturbances in the flow over a range of frequencies. The instability of free shear layers is referred to as Kelvin–Helmholtz (K–H) instability. At sufficiently high Reynolds numbers, the effect of viscosity in the amplification of disturbances is relatively small, and thus this instability is also called inviscid instability. Michalke (1965 & 1977) used linear instability analysis to show that the most amplified frequency, f_n, is directly proportional to the freestream velocity, U_∞, and inversely proportional to the momentum thickness at the trailing edge of the splitter plate θ_0. The Strouhal number based on this was found to be $St_\theta = f_n\theta_0/U_\infty \approx 0.013$. Subsequent experiments (Ho & Huerre 1984) have not only confirmed this, but have also shown that the initial waves due to K-H instability roll up into large-scale coherent structures (Brown and Roshko 1974). These structures entrain the fluid into the mixing layer from both sides and play a major role in bulk mixing of the fluids (Winant & Browand 1974). In the absence of seeded perturbations, natural disturbances do exist in the shear layer but are random in nature; as a result, the process of vortex roll-up and subsequent merging is random too. Therefore, the large-scale structures are not spatially or temporally coherent, and the merging locations are not spatially fixed. By the introduction of a low-amplitude forcing, the events could be manipulated and made much more organized (Winant & Browand 1974; Ho & Huang 1982; Ho & Huerre 1984). Axisymmetric jets add two more complexities to the planar shear layer. The first one arises from azimuthal modes in the axisymmetric shear layer, which compete for energy and grow selectively. The second one arises from the inward growth of the free shear layer toward the jet axis and its eventual interaction around the centerline, which ends the jet potential core.

The ratio of the nozzle exit diameter to the boundary-layer momentum thickness at the nozzle exit (D/θ_0) seems to be the principal factor in deciding which of the azimuthal modes would grow in the jet. Linear stability analysis (Michalke 1965 & 1977; Plaschko 1979) and experimental work (Cohen & Wygnanski 1987; Corke *et al.* 1991; Corke & Kusek 1993) have shown that for large D/θ_0, both the axisymmetric mode ($m_f = 0$) and the first helical mode ($m_f = 1$) are unstable in the initial jet shear layer. Linear stability analysis (Cohen & Wygnanski 1987) also showed that for a very thin boundary layer (or very large D/θ_0), many azimuthal modes are unstable in the initial shear layer region. Michalke (1977) used linear stability analysis to show that farther downstream in the jet, where the velocity profile has gradually changed from being top-hat-shaped to bell-shaped, the jet can only support helical modes. It has also been reported that the growth region of helical modes moves farther upstream toward the nozzle as the jet velocity increases (Ho & Huerre 1984).

In an axisymmetric jet, the inward growth of the jet shear layer and its interaction around the jet axis ends the typical merging of successive large-scale structures and starts an additional interaction: azimuthal interaction. The average location at which the jet centerline velocity begins to decay is called the end of jet potential core. This interaction, which is dynamic and nonlinear, adds tremendous complexity to the problem. Standard linear stability analysis, which has been a guiding light in the understanding of free shear layers and is applicable only in the early development of the shear layer up to roll-up, is no longer helpful. Many researchers have shown experimentally that the passage Strouhal number of large-scale structures at the end of potential core, called the jet preferred mode or jet column mode Strouhal number, scales with the nozzle exit diameter, $St_D = f_pD/U_j \approx 0.2$ to 0.6 (Crow & Champagne 1971; Zaman & Hussain 1980; Reynolds & Bouchard 1981; Hussain & Zaman 1981). Although the St_D seems to vary over a large range, it is often close to 0.3 (Ho & Huerre 1984). Recent experimental results in our laboratory reported in Samimy *et al.* (2007a & b) for high-Reynolds number and Mach 0.9 and 1.3 jets show $St_D \approx 0.3$.

The modern study of jet aeroacoustics started with the work of Lighthill (1952, 1954). In the initial stages, researchers tried to model the noise sources in the Lighthill equation in terms of the random turbulence present in the jet mixing layer (Ffowcs-Williams 1963, Ribner 1969). The scenario was dramatically changed in the late 1960s and early 1970s when the presence of large-scale coherent structures was demonstrated in the axisymmetric jet mixing layer as mentioned above. Researchers soon realized that these structures are important as potential contributors to the radiated far-field noise in addition to the random turbulence (Mollo-Christensen 1967; Crow & Champagne 1971; Lau *et al.* 1972; Fuchs 1972; Brown & Roshko 1974). However, in spite of sustained effort ever since, the exact mechanism of influence has not been pinned down as yet. The following source mechanisms have emerged as popular candidates though: vortex-pairing (Laufer & Yen 1983), wavy-wall type mechanisms (Ffowcs-Williams & Kempton 1978; Crighton & Huerre 1990; Coiffet *et al.* 2006), and vortex eigen-oscillations (Kopiev *et al.* 1999). All of these are believed to be active in the initial mixing-layer region of the flow. An additional postulated mechanism is the violent intermittent events associated with the collapse of the potential core (Juvé *et al.*

1980; Citriniti & George 2000; Bogey *et al.* 2003; Guj *et al.* 2003; Hileman *et al.* 2004; Viswanathan *et al.* 2006). A recent review article by Jordan and Gervais (2008) provides a detailed account of these developments.

An important character of the far-field noise is its directivity. In particular, the noise radiated in the downstream direction is louder than the noise radiated at right angles to the jet exit. This has been predicted by theory (Lighthill 1952; Michalke & Fuchs 1975; Ribner 1981; Kopiev & Chernyshev 1997), and confirmed experimentally (Mollo-Christensen *et al.* 1964; Lush 1971; Stromberg *et al.* 1980) and in direct numerical simulation (Freund 2001). Further, large-scale coherent structures are implicated in the radiation of noise preferentially in the downstream direction (see Tam 1998 and references therein).

From the above discussion, it is clear that the large-scale coherent structures in the jet mixing layer play an important role in mixing as well as noise radiation. In the sequel, we will show that feedback control attempts to manipulate these structures to achieve either one of two desired goals: mixing enhancement or potential noise attenuation.

C. The Near-Field Pressure and its Correlation with Mixing Enhancement and Far-field Noise

In general, jet actuation techniques strive to alter the characteristics of the initial shear layer; for feedback control, a real-time measurement of this effect of forcing is needed. Present technology does not allow real-time 3D measurement of the velocity field in the jet mixing layer. It is also not practical to require direct sensing of far-field noise levels for control applications. In this subsection, we invoke past research efforts to show that the pressure field in the irrotational near-field offers an estimate of both the mixing-layer velocity field as well as the far-field noise. The measurement of the near-field pressure presents some unique opportunities: (i) it is a relatively non-intrusive technique; (ii) pressure, being a scalar variable, is considerably easier to measure than the velocity field inside the flow; and (iii) unlike some of the velocity measurement tools like PIV and PDV, pressure sensors are robust and can be feasibly transferred from the laboratory setting to real-world applications.

For the same reasons as above, researchers seeking a better understanding of the large-scale flow dynamics and its sound production mechanisms have studied the near irrotational pressure field of the axisymmetric jet over the past 50 years. Among them, we mention Mayes *et al.* (1959); Howes (1960); Mollo-Christensen (1963); Keast & Maidanik (1966); Fuchs (1972); Arndt *et al.* (1997); Reba *et al.* (2005); Coiffet *et al.* (2006); Barré *et al.* (2006); and Suzuki & Colonius (2006).

The Poisson equation governs the pressure in the incompressible irrotational near-field of the jet. In analyzing the Green's function solution of the Poisson equation, George *et al.* (1984) found that the mean-square pressure is related to the Reynolds stress by a weighting function $W(k)$ (k being the wavenumber),

$$W(k) = \frac{(4\pi)^2}{|k|^4}.$$

The nature of the rapid roll-off of this weighting function indicates that the pressure spectrum will be dominated by the larger turbulent scales. This is termed wavenumber filtering. Arndt *et al.* (1997), Coiffet *et al.* (2006), and Guitton *et al.* (2007) showed that the near-field pressure consists of two distinct components. The 'hydrodynamic' pressure fluctuations carry the convective footprint of the underlying turbulence in the mixing layer, whereas the 'acoustic' pressure fluctuations are characterized by spherical waves propagating with sonic speed. The far-field is dominated by the acoustic component due to the rapid decay of the hydrodynamic component (Arndt *et al.* 1997). However, in the immediate periphery of the jet, the hydrodynamic component supersedes the acoustic (Arndt *et al.* 1997; Freund 2001; Coiffet *et al.* 2006; Tinney *et al.* 2007). Due to the wavenumber filtering effect, the hydrodynamic pressure itself is dominated by the large-scale coherent structures in the jet mixing layer (Lau *et al.* 1972; Petersen 1978; Arndt *et al.* 1997; Picard & Delville 2000; Ukeiley & Ponton 2004; Hall *et al.* 2005; Coiffet *et al.* 2006; Tinney *et al.* 2007). Thus, in order to detect the behavior of the actuation-modified large-scale structures, the pressure sensors must be positioned close to the mixing layer without actually impinging on it.

An efficient way of looking at the near-field pressure is via its azimuthal modal decomposition (see the Appendix for an explanation of the procedure). Hall *et al.* (2005) measured the near-field pressure of a Mach 0.6 jet using an azimuthal array of 15 transducers; they found the azimuthal pressure spectrum to be dominated by the lower azimuthal modes (0, 1, and 2). Hall *et al.* (2006) also showed that the instantaneous pressure signal can be almost completely reconstructed from the axisymmetric and 1st azimuthal-mode-filtered pressure signals only. The dominance of the lower azimuthal pressure modes was found to increase with downstream distance up to $x/D \approx 3$ and decrease subsequently up to $x/D \approx 6$, before increasing slightly again (Hall *et al.* 2006). This basically demonstrates the low-dimensionality of near-field pressure.

The above discussion shows that the stronger the large-scale structures in the mixing layer, the higher will be pressure fluctuations in the near-field. Since stronger coherent structures have been shown to be associated with

enhanced mixing, this justifies the choice of the near-field pressure signals for estimating the level of mixing in the jet in real-time. However, the relation between the near-field pressure and far-field noise is unclear at this point.

We now refer to correlation studies performed by Hall *et al.* (2006) to ascertain precisely this relationship in a Mach 0.85 and $Re_D = 9.8 \times 10^5$ jet. They placed 6 microphones on a polar array of radius 75D, with polar angles from 15° to 90°, and measured the signals from one of these microphones simultaneously with the pressure measurements on the 15-sensor azimuthal ring array mentioned previously. They found that the axisymmetric mode ($m_p = 0$) of the near-field pressure is better correlated with the far-field noise than just the pressure signal by itself. In particular, they reported a maximum normalized correlation coefficient of 0.34 at $x/D = 7.5$. (For later reference, the correlation coefficient at $x/D = 3$ was found to be 0.11.) The significance of this finding is that the axisymmetric mode of the near-field pressure can be best employed in estimating the far-field noise for feedback control. In contrast, the first helical mode ($m_p = 1$) of the near-field pressure was found to have a very weak correlation with the far-field noise. We have previously mentioned results showing that both modes $m_p = 0$ and $m_p = 1$ are necessary and almost sufficient in recovering the entire near-field pressure signal, the other modes being relatively weaker. The above result shows that of these two modes, only the axisymmetric mode radiates noise efficiently to the far-field.

D. Control of Axisymmetric Jets

Flow control is divided into two general categories: passive and active. Passive control does not add energy to the flow and is often accomplished by geometric modifications. In active control, energy is added to the flow to excite flow instabilities or affect the flow by way of generating new flow structures (e.g., streamwise vortices). Active control is further divided into open loop and closed loop. In the open-loop control, the actuation takes place based on an operator's command or a predetermined input. In the closed-loop (or feedback) control, information from a sensor or sensors in the flow, along with a flow model, guides the actuation process (Gad-El-Hak (2004); Aamo & Krstić (2003); King (2007)).

Open-loop active control can again be divided into two categories. The first category involves energy addition to the flow at a steady rate or at a low-frequency (a frequency that is much lower than any instability frequency in the flow). Some applications of this technique to the control of jets include steady fluidic injection through microjets (Arakeri *et al.* 2003; Krothapalli *et al.* 2003; Castelain 2006) and fluidic chevrons (Henderson *et al.* 2005). These are considered active control due to the energy addition, but they do not have frequency or phase control, which is essential when exciting flow instabilities. The second category involves using actuators with frequency capabilities in the range of flow instability frequencies. This has been achieved using plasma actuators in our laboratory and will be discussed further in this paper.

The majority of the investigations using open-loop control have been carried out in relatively low-speed and low Reynolds number jets. As the speed and the Reynolds number of the jet increase, so do the background noise, the instability frequencies, and the flow momentum. Therefore, actuators must provide excitation signals of much higher amplitude and frequencies. We have recently developed a class of plasma actuators, called localized arc filament plasma actuators (LAFPAs) that can provide excitation signals of high amplitude and high bandwidth for high-speed, high-Reynolds number flow control (Samimy *et al.* 2004, 2007a, 2007b; Utkin *et al.* 2007). These are deployed in an azimuthal array slightly upstream of the jet nozzle exit. The actuators' frequency, phase, and duty cycle (the percentage of time an actuator is on in a cycle for a given frequency) can be controlled independently. In particular, forcing azimuthal mode m_f is achieved by phase shifting the pulse signals to successive actuators by $2\pi m_f / N_f$ radian, where N_f is the number of actuators in the azimuthal array. Therefore, several of these actuators can be used to force the jet column instability, shear layer instability, and various azimuthal modes. In the next subsection, we briefly review the open-loop control work using LAFPAs.

To the best of our knowledge, this paper presents the first instance of the application of closed-loop active control to axisymmetric jets. We will defer a full discussion of the strategy and results until the background has been established.

E. Review of Open-loop Forcing Results using LAFPA

Samimy *et al.* (2007a & b) have reported results of open-loop forcing of axisymmetric jets using LAFPAs; here we review these briefly. Experiments were conducted on a Mach 1.3 and $Re_D = 1.1 \times 10^6$ jet to assess the effect of LAFPAs on the mixing layer (Samimy *et al.* 2007a). Laser-based planar flow visualizations, pressure measurements inside the mixing layer, and two-component PIV measurements were used to evaluate the effects of forcing. The jet responded to the forcing over the entire range of frequencies, but the response was optimum (in terms of generating large-scale coherent structures and mixing enhancement) around the jet preferred-mode Strouhal number of $St_{DF} = 0.33$ ($f_F = 5$ kHz). The jet, with a thin boundary layer ($D/\theta_0 \approx 250$), also responded to the various azimuthal modes explored ($m_f = 0$ to 3, and $m_f = \pm 1, \pm 2, \pm 4$). Forcing the jet with the azimuthal mode $m_f = \pm 1$ at the jet preferred-

mode Strouhal number provided the maximum mixing enhancement, with a significant reduction in the jet potential core length and a significant increase in the jet centre-line velocity decay rate beyond the end of potential core. The flow visualization, growth and decay of perturbations observed in pressure measurements, and PIV data all together showed that the plasma actuators have control authority over such a high-Reynolds-number and high-speed flow.

Experiments were also conducted on a Mach 0.9 and $Re_D = 7.6 \times 10^5$ jet to study the effect of LAFPAs on far-field noise (Samimy *et al.* 2007b). The far-field jet noise was measured using two microphones located at polar angles of 30º and 90º relative to the jet axis along radii of 83D and 45D from the nozzle exit respectively. The first noticeable effect of forcing was the appearance of the forcing tones and its harmonics in acoustic spectra, more prominently for $m_f = 0$ than for $m_f = 3$. More pertinently, both azimuthal modes of forcing resulted in an attenuation of low-frequency noise attended with an amplification of high-frequency noise, at both measurement stations. The directive nature of the far-field noise mentioned earlier was also in evidence with the SPL at 30º being at least 10 dB higher than that at 90º.

A standard metric for comparing broadband noise levels is the overall sound pressure level (OASPL). Samimy *et al.* (2007b) compared the OASPL for the forced jet to the baseline case (the difference is denoted ΔOASPL) with different forcing frequencies and azimuthal modes measured at the two afore-mentioned stations. Several noteworthy features were observed. (i) A well-defined attenuation of noise was evident at high forcing frequencies for all azimuthal forcing modes at both stations. (ii) The forcing Strouhal number corresponding to the minimum OASPL was independent of the forcing azimuthal mode, but varied with the measurement station. At the 30º microphone location, a relatively sharp minimum in ΔOASPL of about –1.2 dB was noted at $St_{DF} \approx 2.0$ ($f_F = 22$ kHz); at the 90º location, a broader minimum of about –0.6 dB occurred at $St_{DF} \approx 3.5$ ($f_F = 39$ kHz). (iii) An amplification of noise was also noted at low forcing frequencies for all azimuthal modes. However, in this regard, the different azimuthal forcing modes had markedly distinct effects.

The above review of open-loop forcing experiments shows that the in-house developed plasma actuators have significant ability to either enhance mixing or attenuate far-field noise, as desired. We next discuss the initial development and implementation of feedback control for these tasks.

F. Extremum-Seeking Scheme for Online Optimization

The previous results reviewed above suggest that the noise attenuation problem can be cast as an optimization problem wherein we seek the forcing frequency that minimizes the far-field noise. It will be shown later that a similar minimum also exists in the near-field pressure. Likewise, the mixing enhancement problem can be recast as a problem of seeking the maximum in the near-field pressure fluctuations. In either case, the optimum forcing frequency will be a function of the operating conditions; for instance, the Mach number and temperature ratio. Open-loop control is unable to cope with this uncertainty since it operates at a preset forcing frequency.

Extremum-seeking (ES) control (Ariyur & Krstić 2003) constitutes a simple and effective methodology for endowing controllers of fixed structure with self-tuning capabilities. ES control is particularly appealing for application in flow control problems (Beaudoin *et al.* 2006, Becker *et al.* 2007, Kim *et al.* 2008) due to the fact that, in principle, a detailed control-oriented model of the plant is not required. This is a particularly useful feature for dynamic systems of interest described by complex and/or uncertain models, as the jet flow considered in this investigation. In ES control, the goal of the feedback control system is to regulate the output variable by on-line optimization of a given cost function. Under nominal operating conditions, this task is accomplished by a model-based controller of fixed structure. In the presence of model uncertainties, since the cost function changes depending on internal conditions and the external environment as mentioned above, an adaptive algorithm is added to the control scheme to iteratively search the space of the controller parameters to determine the input that minimizes (or maximizes) the given cost function. In our previous study of cavity flow control (Kim *et al.* 2008), we have experimentally demonstrated the advantage of ES control over fixed linear-quadratic controllers in terms of overall reduction of sound pressure level and energy consumption, especially when operating in off-design flow conditions.

This brings us full circle back to the motivation for this paper. The axisymmetric mode of the near-field pressure, being well correlated to the far-field noise, will be used for potential feedback minimization of far-field noise. On the other hand, the fluctuations of the sum of the axisymmetric and first helical modes of near-field pressure would be maximized for potential mixing enhancement. ES control will use this information to determine the local gradient of the input/output map in real-time and compute a suitable forcing frequency to optimize the output. The LAFPA control system will then force the jet at the dictated frequency. This sequence will be automatically performed iteratively by the controller for online optimization based on gradient-descent.

II. Experimental Setup

A. Flow Facility

All of the experiments were conducted in the Gas Dynamics and Turbulence Laboratory (GDTL) at The Ohio State University. The ambient air is compressed, dried, and stored in two cylindrical tanks at a pressure of up to 16 MPa with a capacity of 36 m^3. The compressed air is supplied to the stagnation chamber and conditioned before entering into a nozzle. An axisymmetric converging nozzle, which was operated at Mach 0.9, was used. The air is discharged horizontally through the nozzle into an anechoic chamber. The exit diameter of the nozzle is D = 25.4 mm (1.0 inch). A 17.8 mm (0.7 inch) thick nozzle extension, made of boron nitride, was attached to the exit of the nozzle to house the plasma actuators.

The Reynolds number of the jet based on the jet diameter was $Re_D = 7.6 \times 10^5$ for the Mach 0.9 jet. The boundary-layer thickness at the exit of the nozzle is very thin, making it challenging to obtain a boundary-layer profile to determine its momentum thickness and its state. Kastner *et al.* (2004) used a similar converging nozzle and measured a few points within the boundary layer of a Mach 0.9 jet. They estimated the boundary layer to be turbulent, with a thickness of about 1 mm and a momentum thickness of about 0.1 mm. The characteristics of the boundary layer in the current experiments are expected to be quite similar.

B. Near-field Pressure Measurements

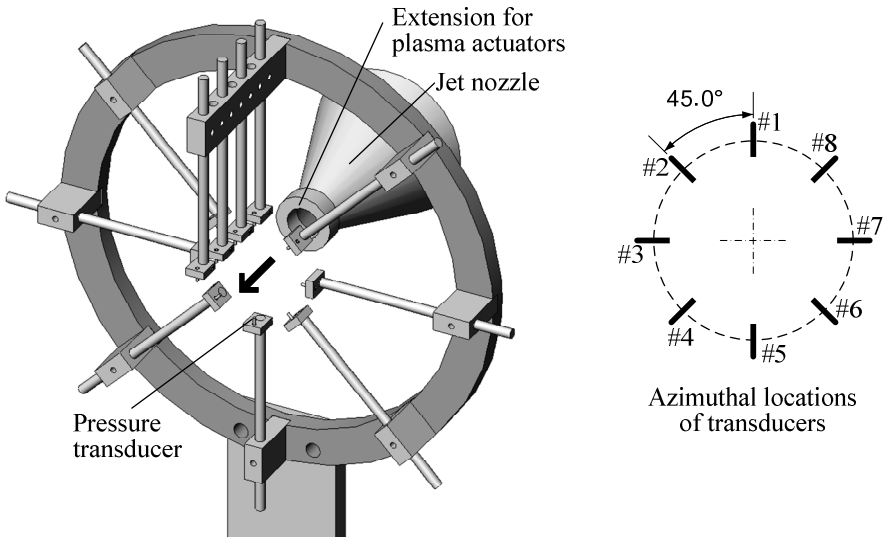

Figure 2. Schematic of near-field pressure sensing using a circular array of eight and a linear array of six pressure transducers.

Figure 2 shows a circular array of N_p = 8 Kulite pressure transducers (model XCQ-062-25A). The inner diameter of the ring that holds the transducers is 254 mm (10 inches), ten times larger than the nozzle diameter. The eight sensors are symmetrically located with an azimuthal separation of 45°. During experiments, the ring was coaxially aligned with the nozzle and could be traversed downstream on a metered slide. This configuration allowed flexibility in choosing the tip-circle radius of the pressure sensors as well as their streamwise location. Additional transducers, a maximum of six, can also be arranged in a linear array aligned with the jet axis with consecutive sensors separated by 12.7 mm (0.5 inch). However, the linear array was not employed in the current experiments.

During baseline unforced experiments and open-loop forcing cases, the pressure signals were amplified, low-pass filtered at 100 kHz, and acquired using an eight channel National Instrument (NI) PCI-6143 ADC card at a sampling rate of 200 kHz. In closed-loop experiments, a dSpace 1103 DSP board operating at 50 kHz sampling rate was used to implement the control algorithm. In these cases the pressure signals were amplified, low-pass filtered at 100 kHz, and then split two ways. One signal from each splitter was connected to the NI board for offline computation of the SPL spectrum in steady-state operation. The other set of signals were again low-pass filtered at

25 kHz before being routed to the input channels of the dSpace board. The dSpace board captured the transient pressure data along with a number of control variables. A schematic of the data flow is shown in Figure 3.

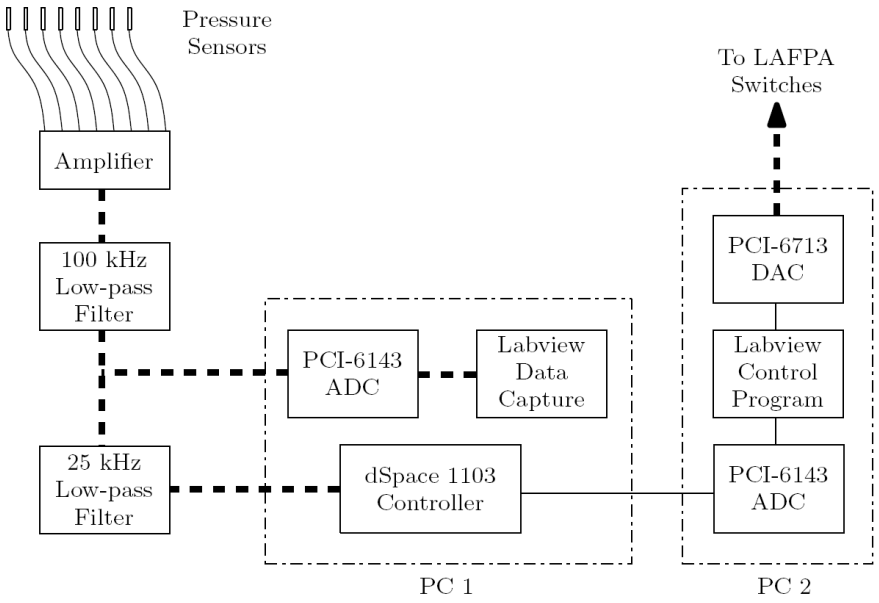

Figure 3. Schematic of data flow in closed-loop experiments. During open-loop forcing cases, the dSpace controller was removed from the loop and the Labview Control Program accepted a user-entry for the forcing frequency to generate the pulses. In baseline experiments, both the dSpace controller as well as PC 2 were disconnected. The heavy dashed lines indicate 8 channels of data flow.

C. Plasma Actuators and Plasma Generator System

Figure 4 shows a schematic of the multichannel high-voltage plasma generator; it was designed and built in-house. Each plasma actuator (LAFPA) consists of a pair of pin electrodes. The electrodes are symmetrically distributed around the perimeter of a boron nitride nozzle extension, approximately 1 mm upstream from the extension exit plane. A 0.5 mm deep and 1 mm wide ring groove was used to house the electrodes and to shield and stabilize the plasma; in the absence of such a groove, the plasma was swept downstream by the flow. Steel or tungsten wires of 1 mm diameter were used for electrodes. Measured center to center at their tips, the spacing between a pair of electrodes comprising an actuator is 3 mm.

The plasma generator enabled simultaneous powering of up to eight plasma actuators with independent frequency, duty cycle, and phase control. Each actuator was connected in series with a fast-response high-repetition-rate high-voltage MOSFET switch; two approximately 15 kΩ high-power solid body ceramic ballast resistors; and a high-voltage high-current (10 kV, 1 A) DC power supply (Glassman High Voltage, Inc.). Two of these power supplies were used to energize the eight actuators. If all eight actuators were powered at the same time, the single actuator current was limited to 0.25 A. The switches were capable of producing high-voltage pulses (up to 10 kV) at repetition rates from a few hertz to 200 kHz, with a very short pulse rise/fall time (~0.1 μs) and a variable duty cycle (from 0 to 100%). Each switch was liquid-cooled to allow continuous operation at high frequency, voltage, and current. A Labview program was used to control the switches through an eight channel NI PCI-6713 DAC card running at an update rate of 780 kHz.

By turning the electronic switch on and off, positive high-voltage pulses are applied to the corresponding actuator. The high initial voltage is needed to produce breakdown in the approximately atmospheric pressure air in the gap between the two electrodes of an actuator. After the breakdown, an arc is generated and the voltage across the gap rapidly falls to a few hundred volts. The plasma generator is compact, robust, and simple to operate.

The duty-cycle *dc* is specified as the percentage on-time of the pulses in each time-period. Previous experiments have shown that optimum performance is achieved by selecting the duty-cycle as

$$dc(\%) = \begin{cases} 0.0006 f_F + 2, & \text{if } f_F \le 30 \text{ kHz} \\ 0.0002857 f_F + 11.4286, & \text{if } f_F > 30 \text{ kHz} \end{cases}$$

This formula is implemented in our actuator control system.

In a typical acoustic driver, which has been used extensively in the literature for flow control, the input signal is a sine wave of prescribed frequency and peak amplitude. On the other hand, the input signal to a plasma actuator is a rectangular wave with a variable duty cycle. Unlike an acoustic driver, the input or forcing amplitude cannot be easily altered in a plasma actuator as it is dictated by the breakdown voltage corresponding to a selected electrode separation. Although the imparted forcing energy to the flow in a cycle can be adjusted by adjusting duty cycle, the effective forcing amplitude is not directly related to the total energy in a cycle. However, due to the same independence of forcing amplitude, it is straightforward to force the jet in any simple azimuthal mode; viz. $m_f = 0, 1, \ldots, N_f/2 - 1$; N_f being the number of actuators used. As mentioned earlier, a forcing azimuthal mode of m_f is achieved by phase shifting the pulse signals to successive actuators by $2\pi m_f / N_f$ radians. The system can also simulate mixed mode forcing; however these were not employed in the current experiments.

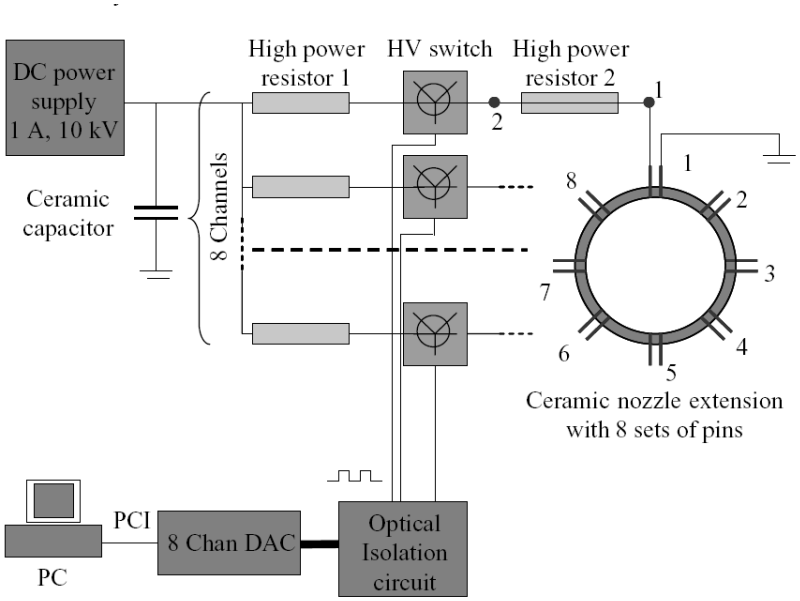

Figure 4. Schematic of the in-house fabricated plasma generator.

D. Interface between Controller and Actuator Hardware

As mentioned previously, the forcing frequency is used as the control input for feedback control. Hence, the Labview program controlling the actuators is required to acquire the time-varying forcing frequency value from an output DAC channel of the dSpace board. The data flow scheme is shown in Figure 3. The PC running the Labview program was embedded with two NI PCI cards. One of them is the eight channel PCI-6713 output DAC card already mentioned. The second was an eight channel PCI-6143 ADC input card (identical to the one used for acquiring the pressure data); only one of its input channels was employed. The input signal from dSpace was sampled at 500 Hz. A higher sampling frequency was deemed unnecessary in view of the other delays in the feedback loop, especially in the algorithm to compute the RMS of the pressure. Over each interval of 2 ms, eight software signal generators created eight packets of pulses at the commanded frequency, one for each actuator. Each packet consisted of 1560 samples to result in the update rate of 780 kHz. These pulses were simultaneously output from the DAC card. Note that the signal generators were run without resetting the phase for each new packet; this is essential for correct operation in a desired forcing azimuthal mode.

III. Baseline Experimental Results

One of the first questions to be answered in our feedback control strategy was the correct positioning of the azimuthal ring array of pressure sensors. In practical applications, one would like to place the sensors as close as possible to the nozzle exit for ease of implementation. However, as mentioned earlier, Hall *et al.* (2006) reported that the correlation of near-field pressure to the far-field noise is low at the jet exit and reaches a maximum at x/D = 7.5. To balance these opposing constraints, we chose to locate our ring array at x/D = 3.0. We have already pointed out that at this location both the axisymmetric and first helical pressure modes have the maximum energy compared to all other streamwise locations (Hall *et al.* 2006). Recall that at this location the correlation coefficient between the near-field pressure and far-field noise is around 0.11. The choice for the tip-circle radius of the pressure sensors is also dictated by conflicting constraints. On the one hand, the pressure sensors should not impinge on the jet to reduce measurement error. On the other hand, as already mentioned, the sensors should be close enough to the mixing layer to capture a strong signature of the hydrodynamic fluctuations in the jet. Kim *et al.* (2007) performed PIV studies of the same jet in the various open-loop forcing experiments; their results show the extent of the jet mixing layer in various forcing conditions. In particular, the maximum radius of the jet at x/D = 3.0 was observed for forcing at the first flapping mode $m_f = \pm 1$; this radius was about 0.9D. Hence, the tip-circle radius was chosen as r = 1.0 D. All near-field pressure data presented in this paper were measured at this location.

A remark is in order about the extreme sensitivity of the near-field SPL to the sensor position. We found that a decrease in the radial distance of $r = 0.03D$ resulted in an increase in the SPL peak by about 1 dB. Hence, extreme care was needed in properly positioning the sensors so that all of them record similar spectra in the unforced case. This was achieved through an iterative calibration procedure. One sensor was located as precisely as possible at the above mentioned location, while the other seven sensors were placed close to their desired location. Then, the SPL was measured at all the sensors and the difference in their spectra was used as a guide for adjustments.

The SPL spectra were calculated from data sampled at 200 kHz using a window size of 8192 samples with a 50% overlap, resulting in a frequency resolution of 24.4 Hz. Each spectrum was obtained by averaging the magnitude of the normalized short-time Fourier transform over 64 such blocks. The data was captured in two blocks of 1.3 s each. The reference pressure for conversion to dB was the standard value of 20 μPa.

Figure 5 presents the spectra for the baseline case. In Figure 5(a), we show that the 8 channels record almost identical SPL spectra. In all subsequent figures where we show the SPL spectra of the pressure, we would refer to the mean SPL of the 8 channels. Figure 5(b) shows the SPL spectra of the first four azimuthal-mode-filtered pressure signals (see the Appendix for a discussion on this topic). At this location, the first helical mode m_p = 1 is the strongest, followed by the axisymmetric mode m_p = 0. The peak pressure is around 3.6 kHz (St_D = 0.33) which corresponds to the jet column instability frequency.

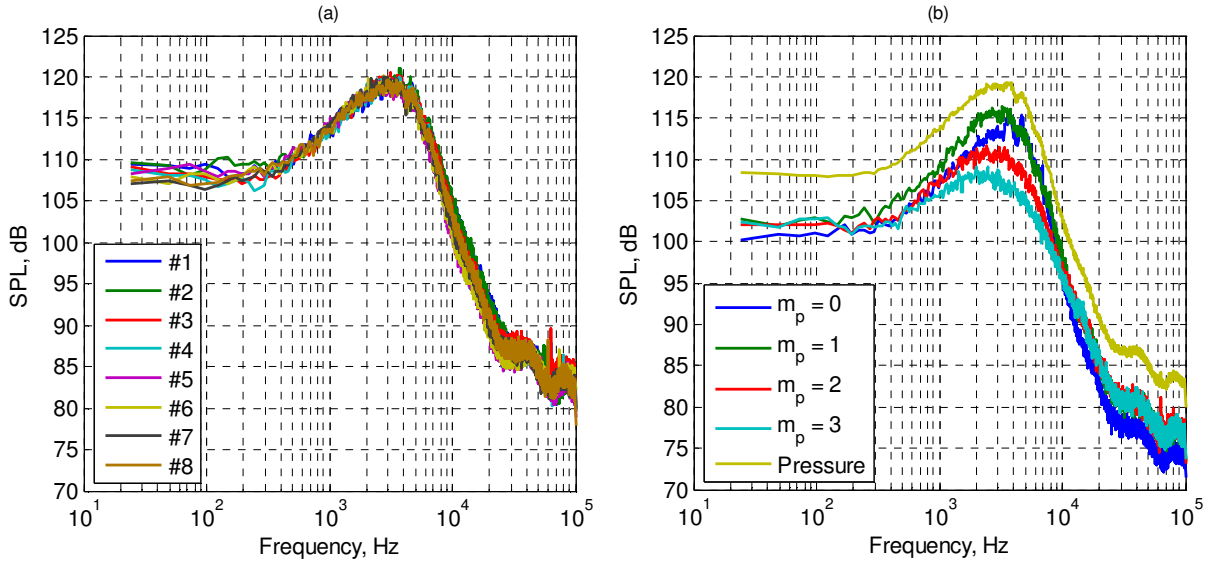

Figure 5. Baseline spectra for (a) individual channels, and (b) various azimuthal modes. Note that the curve marked "pressure" in (b) is the mean of the eight curves in (a).

IV. Open–loop forcing results

The purpose of the open-loop experiments was two-fold. We wished to investigate the effect of forcing on near-field pressure; to our knowledge, this has not been attempted before. We also wanted to trace the static map between the forcing frequency (our control input) and the RMS of the azimuthal-mode-filtered pressure (our control output) to guide the design of the closed-loop controller. Therefore, the data for the open-loop experiments will be presented in terms of the ensemble-RMS values of the pressure signals and its azimuthal-mode-filtered components.

Four different forcing actuation modes were employed, viz. $m_f = 0$, 1, 2, and 3. The forcing frequency was varied in the range f_F = 1 kHz to 60 kHz (St_{DF} = 0.09 to 5.44) in varying step sizes. The azimuthal-mode-filtered pressure signal and its associated SPL were computed in post–processing; see Appendix for a discussion.

Figure 6 shows the SPL spectra for two representative open–loop forcing experiments ($m_f = 0$, f_F = 4 kHz and $m_f = 3$, f_F = 30 kHz) compared to the baseline case. It will be shown that the former corresponds to a maximum in the near-field pressure fluctuations, whereas the latter corresponds to a minimum. The first noticeable aspect is the presence of the forcing tone and its harmonics. The next visible difference is the amplification at the lower forcing frequency and the attenuation at the higher one. Similar effects and trends have been observed in the far-field noise also (Samimy 2007b).

During feedback control, the signals needed to be band-pass-filtered to remove both the DC offset and the high frequency noise. Based on the well-defined broadband peaks in the spectra in Figure 6, we designed a Chebyshev filter with a passband from 0.5 kHz to 8 kHz; its magnitude diagram is shown in Figure 7. For accurate comparison, this filter was also applied to the open-loop pressure signals before computing their RMS values.

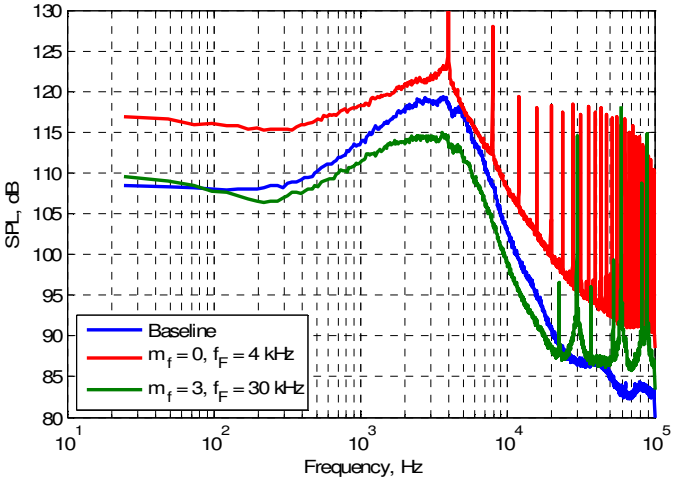

Figure 6. Representative open-loop forcing spectra.

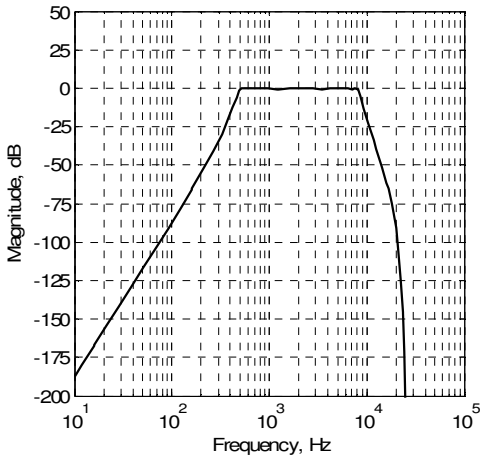

Figure 7. Magnitude plot of bandpass filter.

Figure 8 presents the RMS of the near-field pressure and its various azimuthal-mode-filtered versions for a wide range of forcing frequencies. The following observations can be made regarding these results. (i) Regardless of forcing azimuthal mode, the pressure intensity as well as the intensity of each individual pressure azimuthal mode in the near–field has similar characteristics – there is a relatively sharp maximum at a low f_F and a broad minimum at a higher f_F. Th e maximum clearly corresponds to the jet column-mode instability frequency f_p; earlier flow visualization and PIV results have shown that the jet exhibits the largest response for forcing around this frequency (Samimy *et al.* 2007a). The minimum is more difficult to explain; it is thought to be associated with the initial-shear-layer instability frequency f_n which is predicted to be between 40 kHz and 50 kHz in this case. (ii) Figure 8(a) shows that the peak in the pressure fluctuation intensity is largest for forcing in the axisymmetric mode (m_f = 0) and smallest for forcing in the second and third helical actuation modes (m_f = 2 & 3). It is to be noted that in this regard, forcing at m_f = 3, the highest actuation mode possible in the current setup, is somewhat anomalous compared to the other forcing cases. In particular, the pressure intensity shows a broad peak around f_F = 8 kHz for forcing at m_f = 3, whereas a sharp peak occurs at f_F = 4 kHz for all other forcing cases. (iii) For a particular forcing azimuthal mode m_f, the maximum intensity is noted in the corresponding pressure azimuthal mode m_p. For example, Figure 8(d) shows that the maximum RMS value of the first helical mode of pressure (m_p = 1) is obtained by forcing the jet at the first helical mode (m_f = 1). (iv) The RMS of ($p^{[0]} + p^{[1]}$) shows similar characteristics as the RMS of the pressure for azimuthal forcing modes m_f = 0 and 1, although the actual values are about 50 Pa lower. The same cannot be said

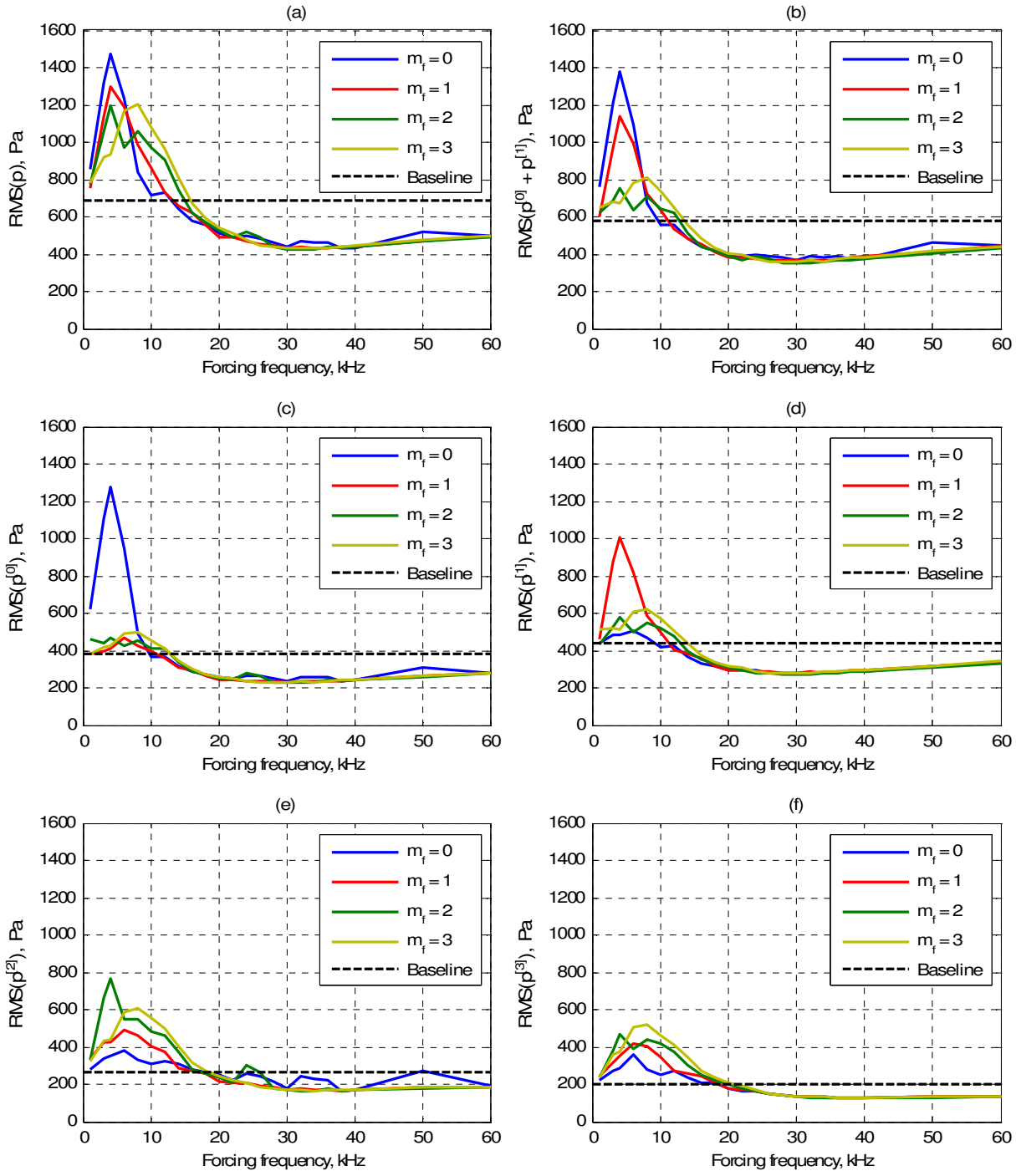

Figure 8. Effect of open-loop forcing on near-field pressure. RMS of (a) pressure, (b) m_p = 0+1, (c) m_p = 0, (d) m_p = 1, (e) m_p = 2, (f) m_p = 3 vs. forcing frequency, f_F. Each graph shows the effect of the four different forcing azimuthal modes explored. Also, the RMS of the respective signals in the baseline case is shown for ease of comparison.

about the forcing azimuthal modes $m_f = 2$ and 3. (v) The switchover from amplification to attenuation (the crossing of the curves with the baseline pressure intensity line) follows a set pattern for the pressure as well as all its azimuthal modes. In particular, the curve for the axisymmetric forcing mode attenuates at the lowest forcing frequency whereas the curve for the third helical forcing mode attenuates at the highest forcing frequency. (vi) The different pressure azimuthal modes also exhibit a progression of crossover locations. For example, all the curves for the axisymmetric pressure mode ($m_p = 0$) crossover at $f_F \approx 10$ kHz (but with differences therein, as mentioned above). However, this crossover happens at at $f_F \approx 20$ kHz for $m_p = 3$. (vii) The effects of different forcing azimuthal modes become indistinguishable at higher forcing frequencies. This is most strikingly visible for the first and third helical pressure modes (Figure 8 (d) and (f)). (viii) The location of the minimum shifts to higher forcing frequencies for increasing pressure azimuthal modes. While the minima for the first two pressure azimuthal modes occur around 30 kHz, those for the 2nd and 3rd helical modes are around 40 kHz. (ix) The minima become flatter, especially on the high-frequency end, for higher pressure azimuthal modes. (x) Since we are relying on the axisymmetric mode of the near-field pressure signal to estimate the far-field noise, it is instructive to compare this result with the effect of forcing on the far-field noise reported by Samimy *et al*. (2007b). They found that the far-field OASPL is minimized at a Strouhal number of $St_{DF} \approx 2$; the corresponding forcing frequency being $f_F = 22$ kHz. On the other hand, Figure 8(c) shows that in the near-field, $p^{[0]}$ is minimized at about 30 kHz. This difference will not be addressed in this paper; here we would minimize RMS($p^{[0]}$) without any reference to the actual far-field noise.

V. Extremum–Seeking Control of Near-field Pressure

Our first effort at feedback control of the irrotational near pressure field of an axisymmetric jet is implemented as an adaptive extremum–seeking algorithm. This is an online gradient-based optimization scheme. The structure of the control system is adopted from Kristić & Wang (2000), and is shown in Figure 9.

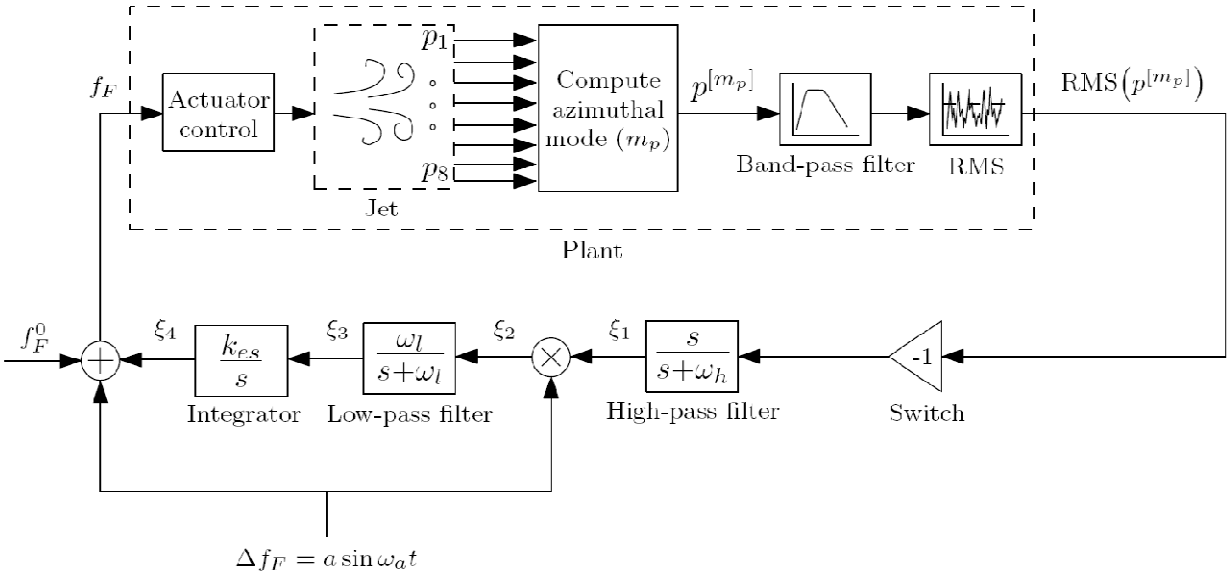

Figure 9. Extremum-seeking control scheme for real-time minimization of jet near-field pressure fluctuations. For maximization of the cost function, the '-1' gain is changed to '+1'.

A. Assumptions

The extremum-seeking control scheme requires very little information about the structure of the plant. However, as for any gradient descent algorithm, one crucial assumption must hold true: the input/output (I/O) map of the plant must have a well-defined extremum that we are attempting to seek closest to the initial guess of the input. For our experiments, the open-loop results presented in the previous section established the maps between forcing frequency as input and the RMS of the various pertinent azimuthal modes of near-field pressure as output. The maps exhibit well-defined extrema and are suitable for the application of gradient-based optimization. The control scheme shown in Figure 9 can be used for both minimum-seeking as well as maximum-seeking by simply switching the gain from –1 to +1.

The second important assumption is regarding the relative dynamics of the plant and controller. For ES control, the plant is defined as shown in Figure 9. In particular, the closed-loop system is considered to be a feedback loop wrapped around a plant seen as a map from the forcing frequency f_F to the RMS of the m_p^{th} pressure azimuthal mode. For the proper operation of the extremum-seeking control, we assume that the dynamics of the plant are much faster than the perturbation dynamics ω_a. In other words, the I/O map is assumed to be static in the controller analysis.

B. The Concept of Extremum-Seeking Control

The following brief analysis is akin to ones presented by Ariyur & Krstić (2003). We will focus on the minimum-seeking scheme; the maximum-seeking is very similar, as mentioned earlier.

Let us denote the plant I/O map by

$$h : f_F \rightarrow \text{RMS}(p^{[m_p]}).$$

The above map will be different for each pressure azimuthal mode considered; however we do not reflect this in h for ease of notation. The forcing frequency can be viewed as the perturbation Δf_F superimposed on the nominal value $\bar{f}_F := f_F^{\,0} + \xi_4$. The static-map assumption allows us to expand $h(f_F)$ in a Taylor series in the vicinity of the nominal value as

$$h(f_F) \approx h(\bar{f}_F) + h'(\bar{f}_F)\Delta f_F = h(\bar{f}_F) + h'(\bar{f}_F)a\sin\omega_a t. \tag{1}$$

Being the output of an integrator, ξ_4 varies much slowly compared to the perturbation. Then, by choosing the high-pass filter cutoff frequency $\omega_h << \omega_a$, the filter output becomes $\xi_1 \approx -h'(\bar{f}_F)a\sin\omega_a t$. The subsequent demodulation by the perturbation signal results in $\xi_2 \approx -h'(\bar{f}_F)a^2/2 + \{h'(\bar{f}_F)a^2\cos 2\omega_a t\}/2$. Selecting the parameter of the low-pass filter $\omega_l << \omega_a$, we find that its output is $\xi_3 \approx -h'(\bar{f}_F)a^2/2$. Finally, the application of the integrator results in the adaptive update law $\dot{\xi}_4 \approx -k_{es}h'(\bar{f}_F)a^2/2$.

We wish to show that the control scheme drives f_F to f_F*, where f_F* is the forcing frequency corresponding to the minimum value of $\text{RMS}(p^{[m_p]})$ nearest to the initial value $f_F^{\,0}$; necessarily, $h'(f_F^{\,*}) = 0$. Consequently, we define the error in the current estimate as $\tilde{f}_F := \bar{f}_F - f_F^{\,*} = (f_F^{\,0} - f_F^{\,*}) + \xi_4$. Then the error dynamic is

$$\frac{d(\tilde{f}_F)}{dt} \approx -k_{es}h'(\bar{f}_F)a^2/2. \tag{2}$$

If all the previous assumptions are valid, then this update law will drive the error to zero and $\text{RMS}(p^{[m_p]})$ will attain its minimum.

It follows that for stable and effective extremum-seeking optimization, the following cascade of frequencies must be established:

$$\begin{aligned}&\text{Sampling frequency of pressure fluctuations} >> \text{Higher end cutoff frequency of bandpass filter}\\ &> \text{Lower end cutoff frequency of bandpass filter} >> \text{Update rate for RMS calculation}\\ &>> \text{Perturbation frequency, } \omega_a >> \text{Filter cutoff frequencies, } \omega_h, \omega_l.\end{aligned} \tag{3}$$

The first and second inequalities are obvious. The third inequality will be discussed in the sequel. The fourth inequality validates the assumption of a static input/output map. The rationale for the final inequality has already been discussed.

C. Choice of Parameters in Extremum-Seeking Control Loop

The real-time RMS computation, which is a component of the augmented plant as shown in Figure 9, will be discussed first. One method of computing the RMS in real-time is to perform a moving-average-like calculation. An offline study of the open-loop experiment results showed that a sample size of about 2000 offers a balance between the need for accuracy and sensitivity of the metric. However, this was beyond the memory capability of the dSpace controller. The other method is to buffer a block of data samples, compute its RMS, use this value as the (constant) output of the algorithm while the buffer is being refilled, and so on. From the offline investigation mentioned above, we decided to use a buffer size of 1500 samples but perform a moving average over 2 such blocks. Note that with a 50 kHz sampling rate of the controller, the effective bandwidth of the plant is then between 16 Hz and 32 Hz.

The choice of the parameters of the extremum-seeking controller is governed by eqn. (3). The perturbation frequency is chosen as 2 Hz, i.e. $\omega_a = 4\pi$ rad/s. This would ensure that the extremum-seeking loop is an order of magnitude slower than the plant. Then, the selection $\omega_h = \omega_l = 0.4\pi$ rad/s ensures that both are an order of magnitude lower than ω_a.

Two parameters remain to be chosen, viz. a and k_{es}. Both of these choices are dictated by a tradeoff between the need for fast convergence and the requirement for the steady tracking of the particular I/O map. The dependence of the convergence rate on these two parameters is evident from eqn. (2). The opposite constraint of steadiness is again tied to the static-map assumption that validates the Taylor series expansion of $h(f_F)$ presented in eqn. (1). Selecting too large a value for either of these parameters will lead to an erroneous estimation of the local slope of $h(f_F)$, thereby causing "hunting".

As presented in Figure 8 and discussed before, the minima and maxima of the I/O maps have very different characteristics. In fact, for the minima, even the high-frequency approach is much more gradual than the approach from the lower frequency end. So, the parameters necessarily need to be chosen differently for optimum performance in these different regimes. While seeking the minima of the I/O maps, the range of f_F was chosen to be from 7 kHz to 63 kHz; also, the breadth of the minima suggests that the control would be relatively insensitive to changes in forcing frequencies in this range. Hence, a suitable choice of the perturbation amplitude for these experiments is a = 1 kHz. On the other hand, the peak in the I/O map being relatively sharp, a choice of a = 350 Hz was found to result in the best performance for maximum-seeking control.

An analysis of eqn. (2) will show that k_{es} has the dimension of Pa^{-1}-s^{-1}. We present a rationale for the choice of k_{es} based on the open-loop forcing results for the axisymmetric pressure mode shown in Figure 8(c). The following analysis is only valid for seeking the minima starting from a low forcing frequency; other cases can be analyzed similarly. Let us assume that starting from an initial frequency of $f_F{}^0$ = 10 kHz, we wish to converge to the optimum frequency $f_F{}^* \approx 30$ kHz in 10 seconds. We estimate $h'(\overline{f}_F)$ as the average of the initial and the final slopes on this I/O map. At f_F = 10 kHz, the slope is around –200 Pa per 10 kHz whereas the final slope is of course zero. Then, using the previously established value of a, we see that the required value of k_{es} is 0.4 Pa^{-1}-s^{-1}. Since the slope is much gentler on the portion of curve to be traced when seeking the minimum starting from a higher frequency, k_{es} necessarily must be chosen larger to obtain faster convergence; the optimum value was found to be 1.0. Finally, the peak being sharper, k_{es} was chosen to be 0.2 for maximum-seeking control to prevent hunting.

VI. Results of Extremum-Seeking Control

A. Minimum-Seeking

We first present results for minimum-seeking. Recall from earlier discussions that the axisymmetric mode of the near-field pressure is best correlated with the far-field noise. Hence, the cost function for minimum-seeking was RMS($p^{[0]}$). Open-loop forcing results presented in Figure 8 have shown that at the high forcing frequency range where the minimum is achieved, the effect of different forcing azimuthal modes cannot be distinguished. However, the I/O map for m_f = 3 being the smoothest, this mode was selected for forcing the jet. As mentioned earlier, the $p^{[0]}$ signal was band-pass filtered between 0.5 kHz and 8 kHz before supplying it to the RMS calculator discussed earlier.

The parameters of the extremum-seeking loop were chosen as mentioned in the previous section. Namely, for seeking the minimum starting from 10 kHz, we used the following set: $\omega_a = 4\pi$ rad/s, $\omega_h = \omega_l = 0.4\pi$ rad/s, a = 1000, and k_{es} = 0.4. When seeking the minimum from the initial frequency of 55 kHz, the only difference was the choice of k_{es} = 1.0 for the reason discussed previously.

Figure 10 presents the performance of minimum-seeking feedback control. Figure 10(a) shows that the forcing frequency was correctly optimized from 10 kHz and settled around 30 kHz within 20 seconds. Higher values of k_{es} were tried to speed up this convergence rate; while they did result in faster convergence (with k_{es} = 1, we could reach 25 kHz within 5 seconds), significant hunting was observed in the long-term behavior. Figure 10(b) shows that the cost function was minimized from 440 Pa to about 230 Pa. A similar minimum can also be observed in the open-loop experiments (see Figure 8(c)). Note that the hunting that was observed in the forcing frequency when higher values of k_{es} were used did not create any corresponding hunting in the cost function. This is to be expected from the broad nature of the minimum in the I/O map.

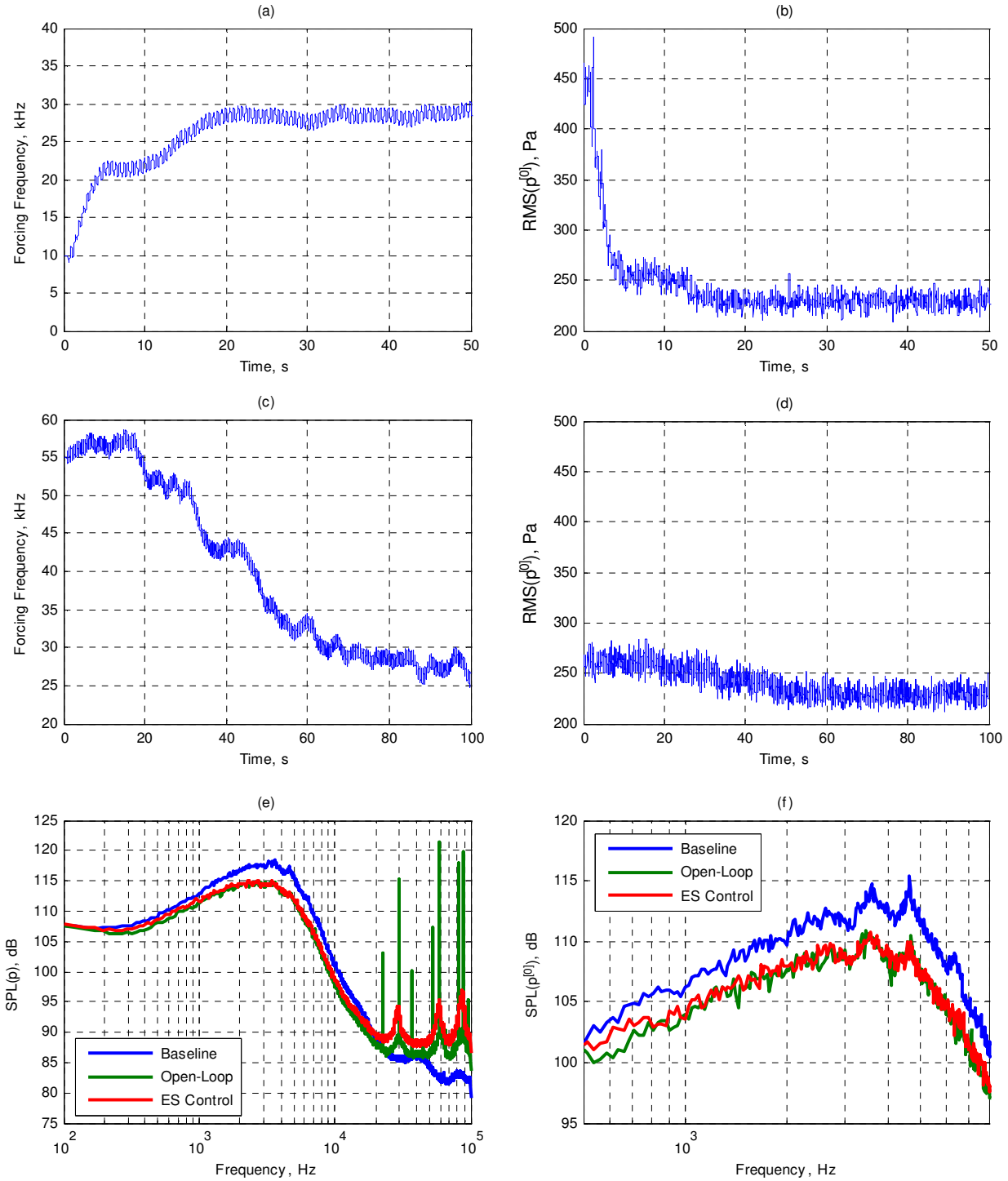

Figure 10. Performance of Minimum-Seeking Control. The forcing azimuthal mode was m_f = 3 and the cost function was RMS($p^{[0]}$). (a) Evolution of forcing frequency starting at 10 kHz. (b) Evolution of cost function for (a). (c) Evolution of forcing frequency starting at 55 kHz. (d) Evolution of cost function for (c). (e) Steady state SPL spectrum of pressure compared with the baseline experiment and the case of open-loop forcing at f_F = 30 kHz & m_f = 3. (f) Steady state SPL spectrum of $p^{[0]}$ compared as in (e). Please see the text for the control parameters. Note the difference in time scales between (a)-(b) and (c)-(d).

Figure 10(c) shows the evolution of the forcing frequency starting from the higher end, viz. 55 kHz. Even with the higher value of k_{es} used in this case (1.0 instead of 0.4), the convergence rate was much slower. The frequency reached ~30 kHz after 80 seconds. Also, some degree of hunting is evident in the long-term behavior owing to this high value of k_{es}. Figure 10(d) shows that the cost function was correctly minimized to 230 Pa starting from 260 Pa.

Figure 10(e) presents the steady state SPL spectrum of the near-field pressure for the case presented in parts (a) and (b). This was identical to the spectrum found in the experiment presented in parts (c) and (d). This spectrum bears a striking resemblance with the one obtained in open-loop forcing at $f_F = 30$ kHz and $m_f = 3$. Compared to the spectrum for the baseline case, there is a broadband attenuation with a reduction of about 5 dB at the peak frequency of 3.6 kHz. The forcing tone and its harmonics in the feedback controlled case are seen to be much smaller, albeit broader, than in the open-loop forcing case due to the persistent perturbations in the forcing frequency. For completeness, Figure 10(f) presents the SPL spectrum of $p^{[0]}$ in the frequency range supplied to the feedback controller; the characteristics are again very similar to the corresponding open-loop spectrum for forcing at 30 kHz. Also, the attenuation compared to the baseline unforced case is noteworthy.

Thus we have hereby demonstrated that minimum-seeking feedback control can automatically replicate the best performance found with open-loop forcing.

B. Maximum-Seeking

As mentioned previously, by changing the gain in the ES loop from –1 to +1, we can use the same setup to seek the maximum of the I/O map. The goal here is mixing enhancement by the maximum amplification of the large-scale structures in the jet shear layer; this in turn is reflected in a broadband increase of the near-field pressure fluctuations. The results from open-loop forcing experiments (see Figure 8) show that the axisymmetric forcing mode ($m_f = 0$) results in the largest amplification of near-field pressure. Hence, all maximum-seeking experiments were performed in this forcing mode. Also, it has been discussed earlier that the near-field pressure is almost fully reconstructed using the sum of its axisymmetric and first helical modes. Hence, the cost function was selected as RMS($p^{[0]} + p^{[1]}$). As before, the ($p^{[0]} + p^{[1]}$) signal was band-pass filtered between 0.5 kHz and 8 kHz before supplying it to the RMS calculator.

The parameters of the extremum-seeking loop were chosen as mentioned in the previous section. Namely, we used the following set: $\omega_a = 4\pi$ rad/s, $\omega_h = \omega_l = 0.4\pi$ rad/s, $a = 350$, and $k_{es} = 0.2$.

Figure 11 presents the performance of maximum-seeking feedback control. Figure 11(a) shows that the forcing frequency was correctly optimized from 10 kHz and settled around 5.2 kHz within 10 seconds. Figure 11(b) shows that the cost function was maximized from 550 Pa to about 1250 Pa. In open-loop forcing experiments presented in Figure 8 (b), the maximum RMS value was found to be 1400 Pa for $f_F = 4$ kHz. This point will be discussed further below. We also found very similar results in experiments to seek the maximum starting from the lower frequency of 1 kHz; they will not be presented here in the interest of brevity.

Figure 11(c) presents the steady state SPL spectrum of the near-field pressure in closed-loop control. This spectrum is shown to be very similar to the one obtained in open-loop forcing at $f_F = 5.2$ kHz and $m_f = 0$. Compared to the spectrum for the baseline case, there is a broadband amplification which is an indication of enhanced mixing. The forcing tone and its harmonics in the feedback controlled case are seen to be much smaller, albeit broader, than in the open-loop forcing case. For completeness, Figure 11(d) presents the SPL spectrum of ($p^{[0]} + p^{[1]}$) in the frequency range supplied to the feedback controller; the characteristics are again very similar to the corresponding open-loop spectrum for forcing at 5.2 kHz.

To investigate the disparity between the optimum open-loop forcing frequency of 4 kHz vis-à-vis the closed-loop steady state frequency of 5.2 kHz, we performed further open-loop experiments with a finer grid of forcing frequencies. In Figure 12, we show the result for RMS($p^{[0]} + p^{[1]}$). Contrary to the indications of Figure 8(b), the I/O map is not smooth in this frequency range. It is surmised that choosing smaller values of a and k_{es} would have allowed the controller to seek the very sharp peak at 3.8 kHz starting from 1 kHz. However, even with the currently selected parameter values, the controller does not have enough perturbations to overcome the local maximum at 5.2 kHz when starting from 10 kHz. Choosing smaller values would have further aggravated this problem. This represents a shortcoming of extremum-seeking control for maximum-seeking for mixing enhancement; viz. the I/O map is not sufficiently smooth in the pertinent forcing frequency range.

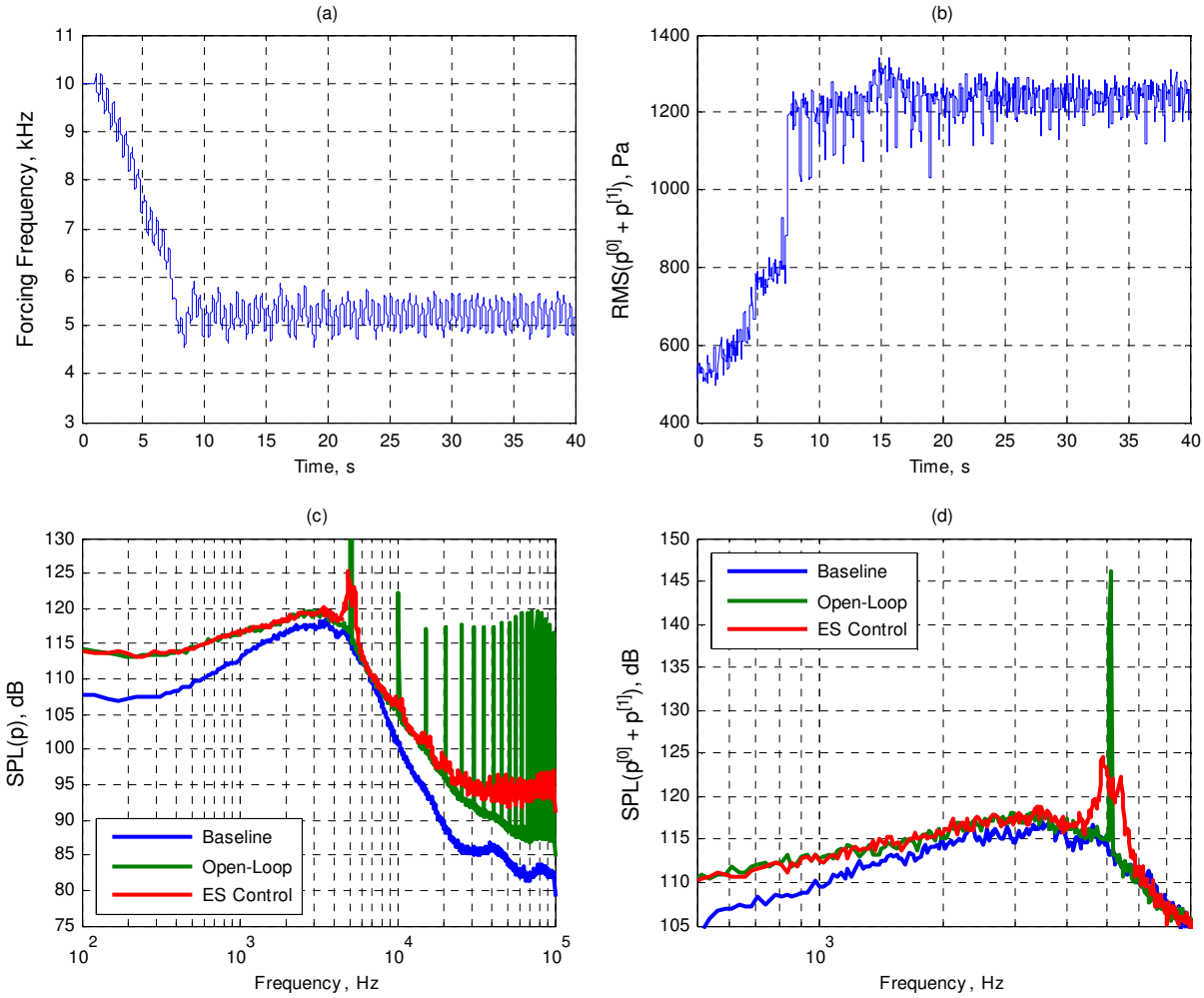

Figure 11. Performance of Maximum-Seeking Control. The forcing azimuthal mode was $m_f = 0$ and the cost function was RMS($p^{[0]} + p^{[1]}$). (a) Evolution of forcing frequency starting at 10 kHz. (b) Evolution of cost function. (c) Steady state SPL spectrum of pressure compared with the baseline experiment and the case of open-loop forcing at $f_F = 5.2$ kHz & $m_f = 0$. (d) Steady state SPL spectrum of ($p^{[0]} + p^{[1]}$) compared as in (c). Please see the text for the control parameters.

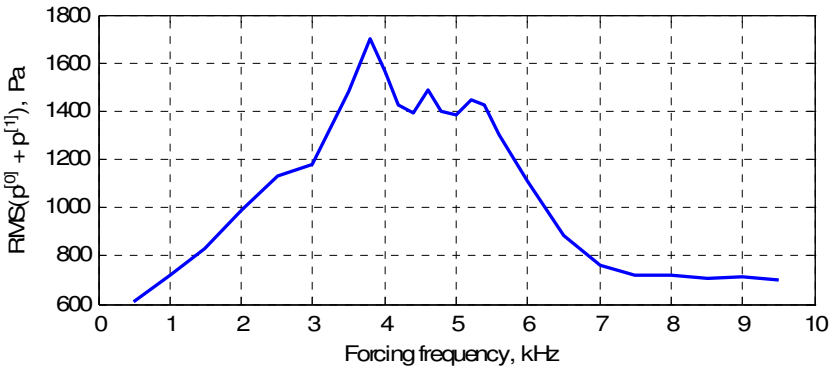

Figure 12. Exploration of the effect of forcing frequency on RMS($p^{[0]} + p^{[1]}$) with a finer grid than in Figure 8. The forcing azimuthal mode is $m_f = 0$.

VII. Conclusion

In this paper we have presented and discussed preliminary results of development and application of feedback control to axisymmetric jets. In particular, we have shown control authority on the near-field pressure of a Mach 0.9 and $Re_D = 7.6 \times 10^5$ jet. To our knowledge, this is the first time that a feedback control strategy in a high-speed and high-Reynolds number jet has been attempted. Open-loop forcing using our in-house developed plasma actuators has been shown to have two distinct effects on the near-field: a sharp peak in the pressure fluctuations occurs at lower forcing frequencies near the jet column mode, whereas a broad minimum is found at higher forcing frequencies. The peak corresponds to optimum mixing enhancement in the jet shear layer; the minimum corresponds to far-field noise attenuation. The optimum forcing frequency for far-field noise attenuation is somewhat lower than the frequency corresponding to the minimum in the near-field pressure fluctuations. In this paper we focus on the near-field only; therefore, this difference is not addressed.

It is shown that azimuthal modal decomposition of the near-field pressure further reveals its structure. Previous research by Hall *et al.* (2006) has shown that the axisymmetric pressure mode is best correlated with the far-field noise; hence, this mode was selected for minimization with a view toward noise attenuation. The same researchers also showed that the near-field pressure is well-reconstructed by the sum of the axisymmetric and first helical pressure modes only; hence, this quantity was selected for maximization for mixing enhancement.

The actual feedback control was implemented as an online gradient-based extremum-seeking scheme. Previously, we have applied this control technique to reduce resonant tones in flow over a shallow cavity (Kim *et al.* 2008). In the current experiments, this controller has been used both for maximum-seeking as well as minimum-seeking. The results presented herein demonstrate that this controller is able to achieve optimum performance in both applications within a relatively short time.

Several open issues need to be addressed in future research. We have already mentioned the difference between the near-field and far-field regarding the minimizing forcing frequency. Another challenge is posed by the non-smoothness of the I/O map near its maximum; in particular, several local maxima are found very close to the global maximum of the map. The current selection of controller parameters has resulted in the closed-loop system getting "trapped" in one of these local maxima. In spite of these issues, extremum-seeking feedback control of jets demonstrates significant promise.

Appendix

A. Azimuthal Modal Decomposition

Azimuthal modal decomposition offers a way to recover essential information from the near-field pressure measurements while filtering out the extraneous components. A statistically stationary time signal can be Fourier-decomposed into its frequency components; similarly, multi-point measurements of a statistically homogeneous flow variable can be decomposed into its spatial modal components. For an axisymmetric jet, the most natural of such decompositions is in terms of its azimuthal modes.

The azimuthal modal decomposition of pressure is performed as follows. We measure the pressure at N_p points on a circle of radius r coaxial with the jet at a given downstream location x. This would be done, for instance, using the ring array of pressure sensors shown in Figure 2. The azimuthal location of the k^{th} sensor is denoted by θ_k, measured from any suitable reference direction. Then the pressure measured at time instant t is defined as $p(r, x, \theta_k, t)$. Typically, we will be focusing on fixed r and x; hence we will actually denote the pressure as $p(\theta_k, t)$. Also, we would assume that the sensors are distributed symmetrically around the circle so that

$$\theta_k = 2\pi(k-1)/N_p, \quad k = 1,\ldots,N_p.$$

At every instant t, a spatial (in azimuthal angle θ_k) Fourier transform is applied to the N_p pressure signals. We arbitrarily choose θ_1 as the reference and obtain the m_p^{th} Fourier azimuthal mode as

$$\hat{p}(m_p,t) = \sum_{k=1}^{N_p} p(\theta_k,t)\mathrm{e}^{-im_p\theta_k}, \quad m_p = 0,\ldots,N_p-1.$$

Due to the symmetric arrangement of the pressure sensors,

$$\hat{p}(-m_p,t) = \{\hat{p}(m_p,t)\}^*$$

where * signifies the complex conjugate. The azimuthal *mode-filtered* pressure signal at the j^{th} sensor is defined as the inverse Fourier transform of the above signal with the undesired modes padded with zeros:

$$\tilde{p}^{[m_p]}(\theta_j,t) := \frac{1}{N_p}\sum_{m_p=0}^{N_p-1}\hat{p}(m_p,t)\mathrm{e}^{im_p\theta_j}, \quad j=1,\ldots,N_p.$$

Typically, we are interested in the signal at the reference sensor; so $\theta_j = 0$. Also, in an axisymmetric jet, it is immaterial whether the m_p^{th} helical mode is clockwise or counter-clockwise. Using the above facts, we define a simple helical mode-filtered signal as

$$p^{[m_p]}(t) := 2\,\mathrm{Re}\{\tilde{p}^{[m_p]}(0,t)\} = \frac{2}{N_p}\mathrm{Re}\{\hat{p}(m_p,t)\} = \frac{2}{N_p}\sum_{k=1}^{N_p} p(\theta_k,t)\cos m_p\theta_k, \quad m_p = 1,\ldots,\frac{N_p}{2}-1.$$

Of course, for the axisymmetric mode, the expression simplifies to

$$p^{[0]}(t) = \frac{1}{N_p}\sum_{k=1}^{N_p} p(\theta_k,t).$$

This is simply the average over the azimuthal array of pressure signals measured at time *t*.

Acknowledgments

The support of this research by the Air Force Office of Scientific Research is greatly appreciated. The authors would like to thank Martin Kearney-Fischer for his help on this project.

References

O. M. Aamo and M. Krstić, *Flow Control by Feedback: Stabilization and Mixing*, Springer, 2003.

V. H. Arakeri, A. Krothapalli, V. Siddavaram, M. B. Alkislar, and L. M. Lourenco. On the use of microjets to suppress turbulence in a mach 0.9 axisymmetric jet. *Journal of Fluid Mechanics*, 490:75–98, 2003.

K. B. Ariyur and M. Krstić. *Real time optimization by extremum seeking control*. Wiley Inter-science, Hoboken, NJ, 2003.

R. E. A. Arndt, D. F. Long, and M. N. Glauser. The proper orthogonal decomposition of pressure fluctuations surrounding a turbulent jet. *Journal of Fluid Mechanics*, 340(1):1–33, 1997.

S. Barré, V. Fleury, C. Bogey, C. Bailly, and D. Juvé. Experimental study of the properties of near-field and far-field jet noise. In *12th AIAA/CEAS Aeroacoustics Conference*, AIAA Paper 2006–2649, 2006.

J.-F. Beaudoin, O. Cadot, J.-L. Aider, and J.-E. Wesfreid. Bluff-body drag reduction by extremum-seeking control. *Journal of Fluids and Structures*, 22(6–7):973–978, 2006.

R. Becker, R. King, R. Petz, and W. Nitsche. Adaptive closed-loop separation control on a high-lift configuration using extremum seeking. *AIAA Journal*, 45(6):1382–1392, 2007.

C. Bogey, C. Bailly, and D. Juvé. Noise investigation of a high subsonic, moderate Reynolds number jet using a compressible large eddy simulation. *Theoretical and Computational Fluid Dynamics*, 16(4):273–297, 2003.

G. L. Brown and A. Roshko. On density effects and large structure in turbulent mixing layers. *Journal of Fluid Mechanics*, 64(4):775–816, 1974.

T. Castelain, J.-C. Béra, and M. Sunyach. Noise reduction of a mach 0.7-0.9 jet by impinging microjets. *Comptes rendus - Mecanique*, 334(2):98–104, 2006.

J. H. Citriniti and W. K. George. Reconstruction of the global velocity field in the axisymmetric mixing layer utilizing the proper orthogonal decomposition. *Journal of Fluid Mechanics*, 418:137–166, 2000.

J. Cohen and I. Wygnanski. The evolution of instabilities in the axisymmetric jet. Part 1. The linear growth of disturbances near the nozzle. *Journal of Fluid Mechanics*, 176(1):191–219, 1987.

F. Coiffet, P. Jordan, J. Delville, Y. Gervais, and F. Ricaud. Coherent structures in subsonic jets: a quasi-irrotational source mechanism? *International Journal of Aeroacoustics*, 5(1): 67–89, 2006.

T. C. Corke and S. M. Kusek. Resonance in axisymmetric jets with controlled helical-mode input. *Journal of Fluid Mechanics*, 249(1):307–336, 1993.

T. C. Corke, F. Shakib, and H. M. Nagib. Mode selection and resonant phase locking in unstable axisymmetric jets. *Journal of Fluid Mechanics*, 223(1):253–311, 1991.

D. G. Crighton and P. Huerre. Shear-layer pressure fluctuations and superdirective acoustic sources. *Journal of Fluid Mechanics*, 220(1):355–368, 1990.

S. Crow and F. Champagne. Orderly structure in jet turbulence. *Journal of Fluid Mechanics*, 48(3):547–591, 1971.

J. E. Ffowcs-Williams. The noise from turbulence convected at high speed. *Proc. R. Soc. Lond. A*, 255(1061):469–503, 1963.

J. E. Ffowcs-Williams and A. J. Kempton. The noise from the large-scale structure of a jet. *Journal of Fluid Mechanics*, 84(4):673–694, 1978.

J. B. Freund. Noise sources in a low-Reynolds-number turbulent jet at Mach 0.9. *Journal of Fluid Mechanics*, 438(1):277–305, 2001.

H. V. Fuchs. Space correlations of the fluctuating pressure in subsonic turbulent jets. *Journal of Sound and Vibration*, 23(1):77–99, 1972.

M. Gad-el-Hak, *Flow Control: Passive, Active, and Reactive Flow Management*, Cambridge Univ. Press, 2004.

W. K. George, P. D. Beuther, and R. E. A. Arndt. Pressure spectra in turbulent free shear flows. *Journal of Fluid Mechanics*, 148(1):155–191, 1984.

A. Guitton, P. Jordan, E. Laurendeau, and J. Delville. Velocity dependence of the near pressure field of subsonic jets: understanding the associated source mechanisms. In *13th AIAA/CEAS Aeroacoustics Conference*, AIAA Paper 2007–3661, 2007.

G. Guj, M. Carley, R. Camussi, and A. Ragni. Acoustic identification of coherent structures in a turbulent jet. *Journal of Sound and Vibration*, 259(5):1037–1065, 2003.

A. M. Hall, M. N. Glauser, and C. E. Tinney. Experimental investigation of the pressure-velocity correlation of a M=0.6 axisymmetric jet. In *35th AIAA Fluid Dynamics Conference and Exhibit*, AIAA Paper 2005–5294, 2005.

J. Hall, J. Pinier, A. M. Hall, and M. N. Glauser. Two-point correlations of the near-field and far-field pressure in a transonic jet. In *Proceedings of FEDSM '06,* FEDSM2006–98458, 2006.

B. Henderson, K. Kinzie, J. Whtimire, and A. Abeysinghe. Impact of fluidic chevrons on jet noise. In *11th AIAA/CEAS Aeroacoustics Conference*, AIAA Paper 2005–2888, 2005.

J. Hileman, B. Thurow, and M. Samimy. Development and evaluation of a 3-D microphone array to locate individual acoustic sources in a high-speed jet. *Journal of Sound and Vibration*, 276:649–669, 2004.

C.-M. Ho and L.-S. Huang. Subharmonics and vortex merging in mixing layers. *Journal of Fluid Mechanics*, 119(1):443–473, 1982.

C.-M. Ho and P. Huerre. Perturbed free shear layers. *Annu. Rev. Fluid Mech*., 16:365–424, 1984.

W. L. Howes. Distribution of time-averaged pressure fluctuations along the boundary of a round subsonic jet. *NASA Technical Note D–468*, 1960.

A. K. M. F. Hussain and K. B. M. Q. Zaman. The 'preferred mode' of the axisymmetric jet. *Journal of Fluid Mechanics*, 110(1):39–71, 1981.

P. Jordan and Y. Gervais. Subsonic jet aeroacoustics: associating experiment, modelling and simulation. *Experiments in Fluids*, 44(1):1–21, 2008.

D. Juvé, M. Sunyach, and G. Comte-Bellot. Intermittency of the noise emission in subsonic cold jets. *Journal of Sound and Vibration*, 71(3):319–332, 1980.

J. Kastner, J. Hileman, and M. Samimy. Exploring high-speed axisymmetric jet noise control using hartmann tube fluidic actuators. In *42nd AIAA Aerospace Sciences Meeting and Exhibit*, AIAA Paper 2004–186, 2004.

D. N. Keast and G. Maidanik. Studies of the near field of noise properties of a small air jet. *Bolt Beranek and Newman, Report 1272*, 1966.

J.-H. Kim, J. Kastner, I. Adamovich, and M. Samimy. Active control of high subsonic jets. In *45th AIAA Aerospace Sciences Meeting and Exhibit*, AIAA Paper 2007–320, 2007.

K. Kim, M. Debiasi, R. Schultz, A. Serrani, and M. Samimy. Dynamic compensation of a synthetic jetlike actuator for closed-loop cavity flow control. *AIAA Journal*, 46(1):232–240, 2008.

R. King (ed.) *Active Flow Control – Papers Contributed to the Conference "Active Flow Control 2006," Berlin, Germany, September 27 to 29, 2006,* Springer, 2007.

V. F. Kopiev and S. A. Chernyshev. Vortex ring eigen-oscillations as a source of sound. *Journal of Fluid Mechanics*, 341(1):19–57, 1997.

V. F. Kopiev, M. Yu. Zaitsev, S. A. Chernyshev, and A. N. Kotova. The role of large-scale vortex in a turbulent jet noise. In *5th AIAA/CEAS Aeroacoustics Conference*, AIAA Paper 1999–1839, 1999.

A. Krothapalli, L. Venkatakrshnan, L. M. Lourenco, B. Greska, and R. Elavarasan. Turbulence and noise suppression of a high-speed jet by water injection. *Journal of Fluid Mechanics*, 491:131–159, 2003.

M. Krstić and H.-H. Wang. Stability of extremum seeking feedback for general nonlinear dynamic systems. *Automatica*, 36(4):595–601, 2000.

J. C. Lau, M. J. Fisher, and H. V. Fuchs. The intrinsic structure of turbulent jets. *Journal of Sound and Vibration*, 22(4):379–406, 1972.

J. Laufer and T. C. Yen. Noise generation by a low-Mach-number jet. *Journal of Fluid Mechanics*, 134(1):1–31, 1983.

M. J. Lighthill. On sound generated aerodynamically. I. General theory. *Proc. R. Soc. Lond. A*, 211(1107):564–587, 1952.

M. J. Lighthill. On sound generated aerodynamically. II. Turbulence as a source of sound. *Proc. R. Soc. Lond. A*, 222(1148):1–32, 1954.

P. A. Lush. Measurements of subsonic jet noise and comparison with theory. *Journal of Fluid Mechanics*, 46(3):477–500, 1971.

W. H. Mayes, W. E. Lanford, and D. H. Hubbard. Near-field and far-field noise surveys of solid-fuel rocket engines for a range of nozzle exit pressures. *NASA Technical Note D–21*, 1959.

A. Michalke. On spatially growing instabilities in an inviscid shear layer. *Journal of Fluid Mechanics*, 23(3):521–544, 1965.

A. Michalke. Instability of compressible circular free jet with consideration of the influence of the jet boundary layer thickness. *NASA TM 75190*, 1977.

A. Michalke and H. V. Fuchs. On turbulence and noise of an axisymmetric shear layer. *Journal of Fluid Mechanics*, 70(1):179–205, 1975.

E. Mollo-Christensen. Measurements of near field pressure of subsonic jets. *NATO A. G. A. R. D. Report 449*, 1963.

E. Mollo-Christensen. Jet noise and shear flow instability seen from an experimenters point of view. *ASME Journal of Applied Mechanics*, E89:1–7, 1967.

E. Mollo-Christensen, M. A. Kolpin, and J. R. Martuccelli. Experiments on jet flows and jet noise far-field spectra and directivity patterns. *Journal of Fluid Mechanics*, 18(2):285–301, 1964.

R. A. Petersen. Influence of wave dispersion on vortex pairing in a jet. *Journal of Fluid Mechanics*, 89(3):469–495, 1978.

C. Picard and J. Delville. Pressure velocity coupling in a subsonic round jet. *International Journal of Heat and Fluid Flow*, 21(3):359–364, June 2000.

P. Plaschko. Helical instabilities of slowly divergent jets. *Journal of Fluid Mechanics*, 92(2):209–215, 1979.

R. Reba, S. Narayanan, T. Colonius, and T. Suzuki. Modeling jet noise from organized structures using near-field hydrodynamic pressure. In *11th AIAA/CEAS Aeroacoustics Conference*, AIAA Paper 2005–3093, 2005.

W. C. Reynolds and E. E. Bouchard. The effect of forcing on the mixing-layer region of a round jet. In R. Michel, J. Cousteix, and R. Houdeville, editors, *Unsteady Shear Flows*, pp 402–411. Springer, 1981.

H. S. Ribner. Quadrupole correlations governing the pattern of jet noise. *Journal of Fluid Mechanics*, 38(1):1–24, 1969.

H. S. Ribner. Perspectives on jet noise. *AIAA Journal*, 19(12):1513–1526, 1981.

M. Samimy, I. Adamovich, B. Webb, J. Kastner, J. Hileman, S. Keshav, and P. Palm. Development and characterization of plasma actuators for high-speed jet control. *Experiments in Fluids*, 37(4):577–588, 2004.

M. Samimy, J.-H. Kim, J. Kastner, I. Adamovich, and Y. Utkin. Active control of high-speed and high-Reynolds-number jets using plasma actuators. *Journal of Fluid Mechanics*, 578: 305–330, 2007a.

M. Samimy, J.-H. Kim, J. Kastner, I. Adamovich, and Y. Utkin. Active control of a Mach 0.9 jet for noise mitigation using plasma actuators. *AIAA Journal*, 45(4):890–901, 2007b.

M. Samimy, M. Debiasi, E. Caraballo, A. Serrani, X. Yuan, J. Little, and J. H. Myatt. Feedback control of subsonic cavity flows using reduced-order models. *Journal of Fluid Mechanics*, 579:315–346, 2007c.

J. Stromberg, D. McLaughlin, and T. Troutt. Flow field and acoustic properties of a Mach number 0.9 jet at a low Reynolds number. *Journal of Sound and Vibration*, 72:159–176, 1980.

T. Suzuki and T. Colonius. Instability waves in a subsonic round jet detected using a near-field phased microphone array. *Journal of Fluid Mechanics*, 565:197–226, 2006.

C. K. W. Tam. Jet noise: Since 1952. *Theoretical and Computational Fluid Dynamics*, 10(1-4): 393–405, January 1998.

C. E. Tinney, P. Jordan, A. M. Hall, J. Delville, and M. N. Glauser. A time-resolved estimate of the turbulence and sound source mechanisms in a subsonic jet flow. Journal of Turbulence, 8(7):1–20, 2007.

L. S. Ukeiley and M. K. Ponton. On the near field pressure of a transonic axisymmetric jet. *International Journal of Aeroacoustics*, 3(1):43–65, 2004.

Y. G. Utkin, S. Keshav, J.-H. Kim, J. Kastner, I. V. Adamovich, and M. Samimy. Development and use of localized arc filament plasma actuators for high-speed flow control. *Journal of Physics D*, 40(3):685–694, 2007.

K. Viswanathan, M. L. Shur, P. R. Spalart, and M. K. Strelets. Computation of the flow and noise of round and beveled nozzles. In *12th AIAA/CEAS Aeroacoustics Conference*, AIAA Paper 2006–2445, 2006.

C. D. Winant and F. K. Browand. Vortex pairing: the mechanism of turbulent mixing-layer growth at moderate reynolds number. *Journal of Fluid Mechanics*, 63(2):237–255, 1974.

K. B. M. Q. Zaman and A. K. M. F. Hussain. Vortex pairing in a circular jet under controlled excitation. Part 1. General jet response. *Journal of Fluid Mechanics*, 101(3):449–491, 1980.